RSC Advances

ROYAL SOCIETY OF CHEMISTRY

www.rsc.org/advances

Graphical and textual abstract:

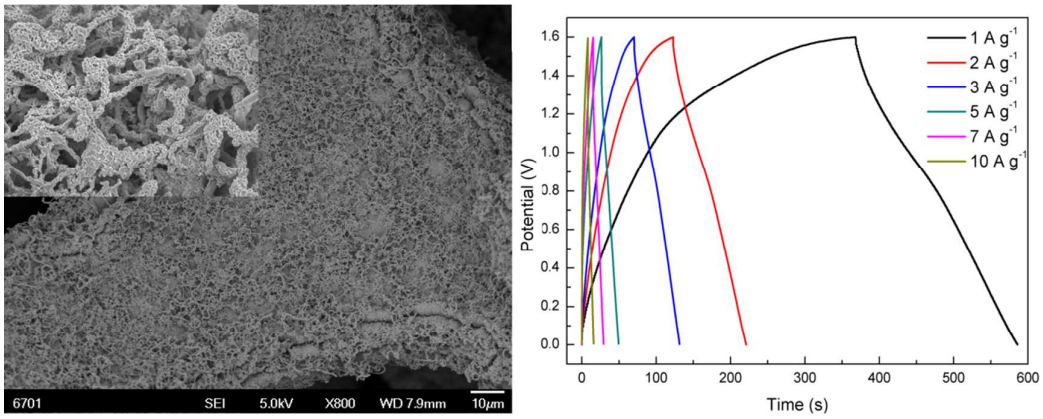

Three-dimensional hierarchical self-Supported $NiCo_2O_4$/Carbon nanotube core-shell network structure shows good supercapacitive performance in both three-electrode and two-electrode cell systems.

Three-Dimensional Hierarchical Self-Supported $NiCo_2O_4$/Carbon Nanotube Core-Shell Networks as High Performance Supercapacitor Electrodes

Xiaocheng Li[a*] *Wei Sun*[a, b], *Liqun Wang*[a, c], *Yongdong Qi*[a,b], *Tieming Guo*[c], *Xinhong Zhao*[b], *Xingbin Yan*[a].

[a]*Laboratory of Clean Energy Chemistry and Materials, Lanzhou Institute of Chemical Physics, Chinese Academy of Sciences, Lanzhou 730000, P. R. China*

[b]*School of petrochemical engineering, Lanzhou University of Technology, Lanzhou 730050, P. R. China.* [c]*State Key Laboratory of Advanced Processing and Recycling of Nonferrous Materials, Lanzhou University of Technology, Lanzhou 730050, P. R. China*

KEYWORDS: Nickel cobaltite; Core-Shell; Supercapacitor; Carbon nanotube; Mesoporous

*Corresponding author. Tel./fax: +86-931-4968040; Email: xiaocheng@licp.cas.cn

ABSTRACT

Three-dimensional (3D) hierarchical self-supported $NiCo_2O_4$/carbon nanotubes/nickel foam ($NiCo_2O_4$/CNT/NF) electrode has been developed by electrodepositing NiCo layered double hydroxides (LDH) on self-supported CNT layer grown on macroporous NF substrate followed by a simple post-annealing process. The resulting 3D hierarchical self-supported $NiCo_2O_4$/CNT/NF electrode delivered high specific capacitances of 1533 F g^{-1} and 1335 F g^{-1} at current densities of 3 A g^{-1} and 30 A g^{-1}, respectively, vastly superior to those of $NiCo_2O_4$/NF electrode at same current density. The $NiCo_2O_4$/CNT/NF electrode also had good cycling stability and showed 102% initial capacitance retention after 2500 cycles at progressively varying current densities. The performance of $NiCo_2O_4$/CNT/NF electrode was further evaluated by two-electrode asymmetric supercapacitor device. The asymmetric device delivered a high energy density of 48.3 Wh kg^{-1} at a power density of 799.9 W kg^{-1} and still remained an energy density of 17.1 Wh kg^{-1} as power density increase up to 7995 W kg^{-1}. Remarkably, the asymmetric device also exhibited good cycling stability with capacitance retention of 78.9% after 2000 cycles at current density of 2 A g^{-1}, indicating the promising applications in supercapacitors. Results of this study also provide an alternative strategy for constructing high performance supercapacitor electrode with high specific capacitance, good rate capability and cycling stability.

Introduction

To address the vast consumption of traditional fossil fuels and causing serious environmental pollution issues, there is an urgent demand to develop sustainable and clean energy sources. Energy storage device, a key component in energy conversion-storage-delivery chain, has attracted much attention and increasing research interest in recent years.[1] Supercapacitors, also known as electrochemical capacitors, are regarded as one of the most promising candidates for use as power resources in various mobile electronic devices and hybrid electric vehicles owing to their high power density, long cycle lifespan and fast charge/discharge rates.[2] In general, two types of supercapacitors exist based on the underlying energy storage mechanisms: carbonaceous compound-based electrical double-layered capacitors (EDLCs), and transition metal oxides/hydroxides-based pseudocapacitors.[3] Unlike that of EDLCs, where the electrostatic adsorption only occurred on the electrode surface, the pseudocapacitors stored energy mainly via fast and reversible redox reactions occurred not only on electrode surface but also in the bulk phase, thus possessing higher capacitance and energy density.[3] Among the transition metal oxide-based supercapacitive materials, hydrous RuO_2 is renowned for its high capacitance of 1580 F g^{-1} and good cycling stability, but the scarcity and toxic in nature seriously impede its commercial applications. Because of these reasons, numerous efforts are being devoted to seeking for alternative cost-effective and environmentally friendly pseudocapacitive materials, especially those who simultaneously possess the multiple redox states and highly reversible redox capability.[4-12]

To date, several possible metal oxides and complex metal oxides, such as NiO,[13-15] Co_3O_4,[16,17] MnO_2,[18-20] Fe_3O_4,[21-23] and $NiCo_2O_4$,[24-28] have been explored for supercapacitor applications. Among them, spinel $NiCo_2O_4$ has been suggested as one of the most promising alternative supercapacitive materials with utilization of two metal oxides. It has been experimentally verified that $NiCo_2O_4$ inherits the advantages of both two metal oxides, and possesses a higher electrical conductivity (at least two orders magnitude) and a higher electrochemical activity than those of single ones.[29, 30] Moreover, spinel $NiCo_2O_4$ is easy to form a mesoporous superstructure, which provides more electroactive sites for faradic reaction and simultaneously offers numerous effective electrolyte-accessible channels for ion transportation. Inspired by these advantageous features, several strategies, including sol-gel,[24,27] hydrothermal,[1,26,31] electrospun[32] and potentiostatic deposition[3,33] have been adopted to synthesize various $NiCo_2O_4$ nanostructures, such as nanoparticle, microsphere, nanosheet, nanowire, nanotube, and $NiCo_2O_4$-based composite. However, in most cases, $NiCo_2O_4$ still suffers from either low capacitance or poor rate capability due to its low intrinsic electrical conductivity. Additionally, the non-conductive polymeric binders used during the electrode fabrication process are also unfavorable to the performance improvement of active materials. Therefore, for $NiCo_2O_4$-based supercapacitors, the simultaneous realization of high capacitance, excellent rate capability and cycling stability is still an ongoing challenge.

It has been proven to be an effective strategy that three-dimensional (3D) hierarchical core-shell network structure, constructed by depositing electroactive

material on highly conductive nanowires or nanotube networks, could make a great contribution to the optimization of electrochemical performance of electrode materials with enhanced specific capacitance, rate capability and cycling stability. Until now, this strategy has been successfully employed to fabricate various 3D core-shell network architectures, such as carbon nanotube (CNT)/MnO_2,[20,34] $Ni_xCo_{2x}(OH)_{6x}$/TiN,[35] CNT/$Ni(OH)_2$,[36] CNT/$Co(OH)_2$,[37] carbon nanofiber/Co_3O_4,[38] carbon nanofiber/MnO_2.[34,39] Among all conductive nanostructured substrates, CNT is a prominent substrate due to its excellent electrical conductivity, high specific surface area and good corrosion resistance in most chemical environments. However, the current research for CNT-supported supecapacitive materials mainly focuses on the simple individual or binary transition metal oxides[4,40-44] and/or hydroxides.[45-48] The investigation on fabrication of complex metal oxide/CNT core-shell composites and their supercapacitive performance exploration has been rarely reported.

Based on the aforementioned considerations, in this study, we construct a 3D hierarchical $NiCo_2O_4$/CNT/nickel foam ($NiCo_2O_4$/CNT/NF) core-shell network electrode via a potentialstatic deposition technique followed by a post-annealing process in air. In this typical binder-free electrode, the CNT networks grown on macroporous NFs are used as "core" to support the mesoporous $NiCo_2O_4$ nanoparticles, which could not only remarkably increase the number of electroactive sites but also notably shorten the electron transport pathway. Meanwhile, the big open interspaces between the CNT/$NiCo_2O_4$ core-shell structures and the nanosized pores in mesoporous $NiCo_2O_4$ superstructure can act as the double buffering reservoirs for

electrolyte, ensuring more interfacial contact between the active material and electrolyte. With these advantageous features, the as-prepared 3D hierarchical $NiCo_2O_4$/CNT/NF core-shell network electrode shows excellent supercapacitive performance in both three-electrode cell system and asymmetric two-electrode cell system.

Experimental details

Growth of CNTs on NF substrate: All chemicals were of analytical grade and directly used as received. NFs (~1.6 mm in thickness, Changsha lyrun Co. Ltd., China) were used as substrate for growth of self-supported CNT layer and also employed as the current collector of supercapacitor electrode. Prior to experiment, NFs were sequentially cleaned with 2% hydrochloric acid, acetone, and deionized water within an ultrasonic bath followed by drying with flowing N_2 gas. CNTs were grown on NFs via a thermal chemical vapor deposition (TCVD) process by using C_2H_2 as carbon source under H_2 atmosphere at a pressure of 20 kPa. The growth time depends on the desired length of CNTs and was set as 20 min in our experiment.

Fabrication and characterization of $NiCo_2O_4$/CNT/NF electrode: Before constructing $NiCo_2O_4$ on CNT backbone, the NF/CNT substrates were treated by air plasma at RF power of 50 W for 20 sec to obtain a hydrophilic surface (Figure S1a and b). The $NiCo_2O_4$/CNT core-shell structure was fabricated by co-electrodepositing of NiCo layered double hydroxides (LDHs) on CNT backbone followed by a thermal annealing process. The co-electrodeposition was performed using a commercial

CHI660E electrochemical workstation (Shanghai Chenhua Instrument Co., China) in a standard three-electrode cell configuration at a cathodic potential of -0.7 V with a saturated calomel electrode (SCE) as reference electrode, a platinum plate as counter electrode and a CNT/NF (1×1 cm^2) substrate as working electrode. The electrolyte was an aqueous solution contained 5 mM $Ni(NO_3)_2$, 10 mM $Co(NO_3)_2$ and 3.75 mM $NaNO_3$. T After deposition, the samples were rinsed with copious deionized water for several times followed by drying at 80 °C for 2 h and finally calcined at 300 ^oC for 2 h with a ramp rate of 1 ^oC/min to transform the NiCo LDHs precursor into $NiCo_2O_4$ nanostructure. For comparison, $NiCo_2O_4$/NF electrode was also fabricated via the same electrochemical deposition procedure. The weight of $NiCo_2O_4$ on CNT/NF and NF substrate was calculated to be 0.78 mg/cm^2 and 0.21 mg/cm^2, respectively, by weighing the substrate before electrodeposition and after thermal annealing process. The as-prepared electrodes were characterized by an X-ray diffractometer (XRD, D/max-2400, Digaku, Japan) with radiation from a Cu target (Kα, λ=0.1541 nm), a field-emission electron microscopy (FESEM; JSM-6701, JOEL) and a high resolution transmission electron microscopy (HRTEM; JEM 2010F, JOEL).

Electrochemical measurements: Cyclic voltammetry (CV) and galvanostatic charge/discharge (CDC) measurements of the as-prepared electrodes were performed on aforementioned electrochemical workstation within a three-electrode cell configuration containing 1 M KOH aqueous solution. The capacitances of the electrodes were calculated from corresponding CDC curves as follows:

$$C_s = I * \Delta t/(\Delta V * m) \quad (1)$$

where C_s (F g^{-1}) is the specific capacitance, I (A) is the discharge current, Δt (s) is the discharge time, ΔV (V) is the window potential during the discharge, and m (g) is the mass of the $NiCo_2O_4$ on NF or CNT/NF current collectors. Electrochemical impedance spectroscopy measurements were carried out at 0.24 V in an alternating current frequency ranging from 0.01 to 3×10^4 Hz with an excitation signal of 5 mV.

Fabrication and electrochemical measurements of asymmetric supercapacitor device: An asymmetric supercapacitor device was assembled using as-prepared $NiCo_2O_4$/CNT/NF electrode as positive electrode, commercial activated carbon (Shanghai Heda Carbon Co., Ltd, China) as negative electrode, commercial cellulose paper as separator and 1M KOH solution as electrolyte, respectively. The capacitance of the as-assembled device is calculated from equation 1 based on the total mass of active materials ($NiCo_2O_4$ and AC) on both two electrodes. The energy density and power density were calculated from following two equations:

$$E = \frac{C \cdot \Delta V^2}{7.2} \quad (2)$$

$$P = E \times 3600/t \quad (3)$$

where E (Wh kg^{-1}) and P (W kg^{-1}) are energy density and power density, respectively. The definitions of C, ΔV and t are the same as those in equation 1.

Results and discussion

Construction of core-shell structure has been proven to be an efficient strategy to improve the electrochemical performance of supercapacitor electrode. Here this strategy is realized by depositing NiCo LDHs precursor on self-supported CNT networks grown on NF followed by a post-annealing process. Figure 1a shows the FESEM image of CNTs grown on NFs. It was found that after the typical self-catalytic TCVD process a thin layer of hairy CNT film was uniformly grown on macroporous 3D NF skeleton along all direction and formed a 3D micro/nano hierarchical structure. The inset of figure 1a indicated that the grown hairy CNT layer consisted of randomly orientated, entangled CNTs with diameter ranging from 40-200 nm, forming a self-supported highly conductive 3D network structure via the underlying NF skeleton. Undoubtedly, the grown CNT layer greatly increases the surface area of NF. Considering its good electrical conductivity and excellent anti-corrosion properties, the grown CNT layer is expected to serve as a good skeleton to support NiCo LDHs supercapacitive materials and as a good current collector for supercapacitor electrode.

The electrodeposition of NiCo LDHs on CNTs in our study mainly involved the reduction of NO_3^- to produce the OH^- ion in the vicinity of cathodic surface and the subsequent precipitation of NiCo LDHs precursor on CNT backbone due to the approximately equal solubility product constant (*K*sp) of $Co(OH)_2$ (2.5×10^{-16}) and $Ni(OH)_2$ (2.8×10^{-16}).[30] The whole electrodeposition process can be described as following two equations:

$$NO_3^- + H_2O + 2\,e^- \rightarrow NO_2^- + 2OH^- \quad (4)$$

$$xNi^{2+} + 2xCo^{2+} + 6xOH^- \rightarrow Ni_xCo_{2x}(OH)_{6X} \quad (5)$$

The electrodeposited green NiCo LDHs precursor can be thermally converted into black $NiCo_2O_4$ loaded on CNT backbone via a typical oxidation reaction expressed as follows:

$$Ni_xCo_{2x}(OH)_{6X} + \tfrac{1}{2}O_2 \rightarrow xNiCo_2O_4 + 3xH_2O \quad (6)$$

Figure 1b-d shows the FESEM images of the as-prepared $NiCo_2O_4$/CNT/NF electrode. As demonstrated, after thermal treatment, the NF substrate was uniformly covered with 3D $NiCo_2O_4$/CNT network structure, roughly preserving the morphology of CNT networks before electrochemical deposition (Figure 1b). High magnification FESEM images, as shown in figure 1c-d, indicated that $NiCo_2O_4$ nanoparticles were tightly adhered on the sidewall of CNTs, forming a core-shell network structure with open space size ranging from several hundred nanometers to several micrometers. By contrast, the $NiCo_2O_4$ directly grown on NFs via the same fabrication procedure, as shown in figure S2a-b, was densely packed together and demonstrated a rather discrete distribution of intercrossed nanoflakes with pore size ranging from 100-300 nm, leading to a much reduced specific surface area. Figure 2 shows the XRD pattern of $NiCo_2O_4$/CNT/NF electrode. As demonstrated, except for the peaks of CNTs and NF substrate, several well-defined diffraction peaks were clearly observed at 2θ values of 18.8°, 36.6°, 44.5°, 55.5°, 59.1°, and 64.9 °, which can be indexed as the (111), (311), (400), (422), (511) and (440) plane reflections of the

spinel $NiCo_2O_4$ crystalline structure (JCPDS: 20-0781), respectively. This indicates that the $NiCo_2O_4$ shell layer deposited on CNT core has the spinel crystalline structure with nickel located at octahedral sites and cobalt occupied both octahedral and tetrahedral sites[1]; see figure 2b. The broadening of the XRD peaks in figure 2a is correlated to the small crystallite size of the synthesized $NiCo_2O_4$, which is expected to have a higher electrochemical activity. According to Scherrer formula, the average crystallite size of the synthesized $NiCo_2O_4$ was calculated to be about 14.5 nm by analyzing the (311) peak in XRD pattern.

The detailed microstructure of the synthesized $NiCo_2O_4$ layer was characterized by using HRTEM. As shown in figure 3a, the $NiCo_2O_4$ nanoparticles observed in FESEM image actually consisted of randomly orientated mesoporous $NiCo_2O_4$ nanocrystals with size ranging from 5 to 20 nm and pores with size ranging from 2 to 8 nm. Further analysis results indicated that the interspacing distance between adjacent fingers in regions 1, 2 and 3 was 0.24, 0.47 and 0.29 nm, respectively, which are in a good agreement with the theoretical interplane spacing of (311), (111) and (220) planes of spinel $NiCo_2O_4$ (figure 3b-d), respectively. Selected-area electron diffraction (SAED) pattern, as shown in figure 3e, demonstrated the well-defined diffraction rings, suggesting the polycrystalline characteristics of $NiCo_2O_4$ nanoparticles. All above observations confirm the successful formation of nanosized mesoporous $NiCo_2O_4$ crystallites on 3D CNT backbone in our experiment.

XPS technique was used to investigate the chemical state of the as-prepared $NiCo_2O_4$/CNT/NF electrode in our study. As shown in figure 4a, the survey spectrum indicated the presence of Ni, Co, O, and C element from CNTs, as well as the absence of other impurities. Figure 4b and c gives the Ni 2p and Co 2p emission spectra, respectively. By using the Gaussian fitting method, the Ni 2p emission spectrum can be fitted as two spin-orbit doublets and two shakeup satellites (indicated as "Sat."). The deconvoluted Ni $2p_{3/2}$ spectrum showed a peak at 854.6 eV corresponding to the Ni^{2+} ions located in the octahedral sites and a peak at 855.5 eV corresponding to Ni^{3+} ions located in tetrahedral sites, while the shakeup satellite peak centered at 860.8 eV was related to both Ni^{2+} and Ni^{3+} ions. Similarly, the Co 2p emission spectrum also can be fitted into two spin-orbit doublets, characteristics of Co^{2+} and Co^{3+}, and two shakeup satellites. All these facts imply that the chemical composition of as-prepared $NiCo_2O_4$ contains Ni^{2+}, Ni^{3+}, Co^{2+}, and Co^{3+}, which is consistent with the results in literature.[1,27,49]

CV and galvanostatic CDC measurements were employed to characterize the electrocapacitive performance of the as-prepared two electrodes. Figure 5a and b shows the CV curves of $NiCo_2O_4$/NF electrode and $NiCo_2O_4$/CNT/NF electrode at various sweep rates, respectively. It can be observed that all CV curves of $NiCo_2O_4$/NF electrode at various sweep rates were characterized by a pair of well-defined redox peaks derived from the faradic reaction expressed as follows:

$$NiCo_2O_4 + OH^- + H_2O \Leftrightarrow NiOOH + 2CoOOH + e^- \qquad (7)$$

while for the CV curves of $NiCo_2O_4$/CNT/NF electrode, besides the obvious redox peaks between 0.2-0.6 V, the typical rectangular shaped regions were also clearly observed within potential range of 0-0.2 V. According to previous reports,[50,51] the rectangular regions were closely related with the electrical double layer between the $NiCo_2O_4$ and hydroxyl ions, which can be expressed as following equation:

$$NiCo_2O_4 + OH^- \Leftrightarrow NiCo_2O_4 \parallel OH^- \quad (8)$$

where $NiCo_2O_4 \parallel OH^-$ represents the electrical double layer formed on electrode/electrolyte infterface. These suggest that both EDLCs and faradic reactions are involved during the energy conversion process of $NiCo_2O_4$/CNT/NF electrode. To evaluate the contribution of EDLCs from CNTs, we compared the CV curves of $NiCo_2O_4$/CNT/NF electrode and NF/CNT substrate at sweep rate of 10 mV s^{-1}. As demonstrated in figure 5c, CV curve of CNT/NF substrate, in contrast to that of $NiCo_2O_4$/CNT/NF electrode, was nearly a horizontal line along the potential-axis, indicating an extremely low EDLCs value. Therefore, the remarkable EDLCs behavior of $NiCo_2O_4$/CNT/NF electrode is mainly resulted from the reversible adsorption of electrolyte ions on surface of mesporous $NiCo_2O_4$ rather than from CNT/NF substrate. Although the CNT layer has the negligible contribution to capacitance of $NiCo_2O_4$/CNT/NF electrode, it provides a highly conductive skeleton for depositing mesoporous $NiCo_2O_4$ and enables the formation of $NiCo_2O_4$/CNT core-shell networks. Additionally, the peak potential of $NiCo_2O_4$/CNT/NF electrode shifted only ~50 mV for a five-time increase in sweep rate range, suggesting the

superfast electronic transport rate and good rate capability of the $NiCo_2O_4$/CNT/NF electrode.

Series galvanostatic CDC measurements were performed on the two as-prepared $NiCo_2O_4$ electrodes in 1 M KOH electrolyte within the potential window of 0-0.5 V at current densities ranging from 3 to 30 A g^{-1}. As shown in figure 6a and b, the shape of CDC curves of $NiCo_2O_4$/NF electrode and $NiCo_2O_4$/CNT/NF electrode had a notable difference. The CDC curves of $NiCo_2O_4$/NF electrode at various current densities were similar to those in previous reports and demonstrated the characteristics of purely capacitive behavior (figure 6a). While for the CDC curves of $NiCo_2O_4$/CNT/NF electrode, as shown in figure 6b, they can be divided into two distinct regions: a linear region between 0-0.2 V and a voltage plateaus between 0.2-0.5 V. The capacitance within the linear region mainly originated from the EDLCs formed on interface of mesoporpous $NiCo_2O_4$/electrolyte, while the capacitance within the voltage region mainly resulted from the interfacial faradic redox couples of Ni^{2+}/Ni^{3+} and Co^{2+}/Co^{3+}. Undoubtedly, the pseudocapacitance still plays the dominant role in the electrochemical capacitance of $NiCo_2O_4$/CNT/NF electrode because the discharging time of the plateau region is much longer than that of the linear region. The capacitance values of two electrodes at various current densities were calculated based on their corresponding CDC curves and are plotted in figure 6c. Encouragingly, the $NiCo_2O_4$/CNT/NF electrode delivered the high capacitance of 1533, 1492, 1446, 1384 and 1335 F g^{-1} at current densities of 3, 5, 10, 20 and 30 A g^{-1}, respectively. This indicates that about 87% of capacitance is still

remained as the current density increases from 3 to 30 A g^{-1}, suggesting the superb rate capability. In contrast, although the $NiCo_2O_4$/NF electrode also delivered the good rate capability, its specific capacitances were very low and only reached about one half of those of $NiCo_2O_4$/CNT/NF electrode at the same current density. The capacitance and rate capability of such integrated binder-free 3D hierarchical $NiCo_2O_4$/CNT/NF core-shell structured electrode are also superior to those of most of slurry-derived $NiCo_2O_4$-based electrode (such as nanowire,[24] hollow microspheres,[30] flower-like[52] and $NiCo_2O_4$/graphene composite[53]) and self-standing $NiCo_2O_4$ nnaostructure-based electrode[50,54-56] with roughly the same mass loading level (see Table S1). All these further confirm the advantages of the $NiCo_2O_4$/CNT core-shell network structure in achieving both high specific capacitance and superb rate capability.

The enhanced electrochemical performance of $NiCo_2O_4$/CNT/NF electrode is intrinsically associated with its special core-shell structure and can be confirmed by EIS measurements (Fig. S3). The EIS spectrum of $NiCo_2O_4$/CNT/NF electrode demonstrated lower charge-transfer interfacial resistance (R_{ct}) at high-/medium frequency region (the semicircle with smaller diameter) and lower diffusion resistance at low frequency region (the straight line with stiffer slope). The lower charge transfer resistance suggests the faster faradic response and greater distribution of electric double layer at electrode interface, two of which closely depend on the large electroactive surface area of mesporous $NiCo_2O_4$ nanoparticles deposited on 3D self-supported CNT network. Additionally, the formation of $NiCo_2O_4$/CNT core-shell

network structure is also favorable for lowering of R_{ct} by providing large amount of highly conductive channels for charge transportation and simultaneously shortening the charge transportation pathway from active material to current collector. All these results are in good agreement with the their CV and CDC behaviors, which clearly demonstrate that $NiCo_2O_4$/CNT/NF electrode can deliver higher faradic capacitance and more pronounced EDLCs as compared to those of $NiCo_2O_4$/NF electrode.

Long-term cycling performance, especially at progressively increasing current densities, which can more precisely reflect the stability of supercapacitor, was also investigated in this study. Figure 6d shows the cycling performance of the as-prepared $NiCo_2O_4$/CNT/NF electrode subjected to continuous charging/discharging for 2500 cycles at various current densities. As demonstrated, the capacitance of $NiCo_2O_4$/CNT/NF electrode gradually increased up to 1759 F g^{-1} during the initial 500 cycles at a current density of 3 A g^{-1}, which can be attributed to the full activation of the electrode. After that, the capacitance gradually decreased and still delivered a high capacitance of 1728 F g^{-1} at 1000^{th} cycles. As the current density was progressively increased up to 5 and 10 A g^{-1}, the $NiCo_2O_4$/CNT/NF electrode also exhibited the good capacitance stability with more than 94% retention at each 500 cycles. After continuous cycling test for 2000 cycles at progressively varying current densities, the current density was turned back to 3 A g^{-1}. Surprisingly, a high capacitance of 1628 F g^{-1} still can be delivered and maintained another 500 cycles with a low capacitance loss of 4%. By and large, the as-prepared $NiCo_2O_4$/CNT/NF electrode demonstrated the excellent cycling stability and delivered about 102% initial

capacitance retention (or 88% retention of maximum capacitance) after 2500 cycles at various current densities, superior to that of $NiCo_2O_4$/NF electrode in this work and those of most $NiCo_2O_4$-based electrode in literature (see Table S1). The excellent cycling performance of $NiCo_2O_4$/CNT/NF electrode is mainly attributed to the advanced self-supported CNT/$NiCo_2O_4$ core-shell network structure and the good adhesion between the $NiCo_2O_4$ nanoparticles and CNT skeleton. This advanced electrode design concept is also can be easily extended to construct other hierarchical 3D metal oxide or metal hydroxide/CNT supercapacitive electrodes.

To further evaluate its capacitive performance for practical applications, asymmetric device was assembled using as-prepared 3D hierarchical $NiCo_2O_4$/CNT/NF electrode as positive electrode, commercial activated carbon (AC) as negative electrode, commercial cellulose paper as separator and 1M KOH solution as electrolyte, respectively. Based on the capacitance values of positive $NiCo_2O_4$/CNT/NF electrode (figure 6b) and negative AC electrode (figure S4) as well as their corresponding potential windows, the mass ratio of $NiCo_2O_4$ and AC was set to be 0.31 to balance the charges stored in both two electrodes. Figure 7a shows the CV curve of the assembled device within the different potential windows. As demonstrated, the assembled device exhibited highly reversible energy storage behavior within potential window of 0-1.6 V and an obvious oxygen evolution reaction-induced irreversible process within potential window of 1.6-1.8 V. Therefore, the potential window of 0-1.6 V was chosen for further investigation of the overall electrochemical performance of assembled asymmetric device. Figure 7b shows the

CV curves of the assembled device at various scan rates from 10-30 mV s^{-1} within the potential window of 0-1.6 V. Obviously, all the CV curves of the device behave similarly in shape and demonstrate a profile close to the rectangular shape with a pair of light redox peaks located at 1.3/0.95 V, different from those of individual AC and $NiCo_2O_4$/CNT/NF electrode. The possible reason is that the hybrid capacitor device integrates the performance of both two electrodes into a mutual complementarity system. It also can be observed that the current density of the device increases approximately linearly with the square root of the scan rate (see figure S5), indicating the diffusion-controlled energy storage process. Based on the CDC curves (inset of figure 7c) and total mass of active materials on both two electrodes, the capacitances of the assembled device were calculated via the equation 1 and are plotted in figure 7c. As demonstrated, the assembled device delivered a high cell capacitance of 135.8 F g^{-1} at a current density of 1 A g^{-1}, and still remain a moderate capacitance of 48.1 F g^{-1} as current density increase up to 10 A g^{-1}. Energy density and corresponding power density of the device were calculated on the CDC curves and the results are demonstrated as a Ragone plot in figure 7d. The assembled device delivered a high energy density of 48.3 Wh kg^{-1} at a power density of 799.9 W kg^{-1}. Encouragingly, the assembled device still can remain as high as 17.1 Wh kg^{-1} even at a high power density of 7995 W kg^{-1} with energy retention of 35.4% for the power density increase nearly 10 times, suggesting good practical performance. It should be noted that the commercial AC with moderate capacitance value of 275 F g^{-1} at current density of 1A g^{-1} was used as negative electrode, seriously limiting the performance of the

assembled device. In the future, if coupled with negative electrode with higher capacitive permance, such as N-doped activated carbon which has the high capacitance of 300-500 F g^{-1},[57] higher cell energy density would be expected for $NiCo_2O_4$/CNT-based asymmetric supercapacitor. The repeated CDC measurement at current density of 2 A g^{-1} was used to evaluate the durability of the as-assembled device. As shown in figure 8, the device can remain about 78.9% of its original capacitance even after 2000 cycles, further confirming its promising application in supercapacitors.

Conclusions

We have successfully developed a 3D hierarchical $NiCo_2O_4$/CNT/NF electrode via a facial and scalable three-step fabrication route. The resulting $NiCo_2O_4$/CNT/NF electrode displayed a typical hierarchical core-shell network structure with mesoporous spinel $NiCo_2O_4$ loaded on self-supported CNT layer. Owing to its special core-shell network structure, the $NiCo_2O_4$/CNT/NF electrode delivered the high specific capacitance, good rate capability and excellent cycling stability at progressively varying current densities. With the as-prepared $NiCo_2O_4$/CNT/NF electrode as positive electrode and commercial AC as negative, the assembled asymmetric supercapacitor device delivered high power density and energy density as well as good cycling stability, suggesting the promising applications in supercapacitors. In the future, if coupled with negative electrode material with higher capacitance, the energy density and power density of the device can be further greatly

improved. Predictably, the developed synthetic methodology and strategy for constructing $NiCo_2O_4$/CNT/NF electrode can be easily extended to prepare series 3D hierarchical metal oxide or metal hydroxide/CNT architectures as highly active materials for fuel cells, batteries and more specifically for applications in rechargeable supercapacitors.

ACKNOWLEDGMENT

Dr. X. Zhao thanks the financial support offered by the National Natural Science Foundation of China (Grant No. 21306072).

REFERENCES

[1] L. Shen, Q. Che, H. Li, X. Zhang, *Adv. Funct. Mater.*, 2014, 24, 2630-2637.

[2] G. Zhang, X.W. Lou, *Sci. Rep.*, 2013, **3**, 1470.

[3] J. B. Wu, R. Q. Guo, X. H. Huang, Y. Lin, *J. Power Sources*, 2013, **243**, 317-322.

[4] M. Zhi, C. Xiang, J. Li, M. Li, N. Wu, *Nanoscale*, 2013, **5**, 72-88.

[5] D. Han, P. Xu, X. Jing, J. Wang, D. Song, J. Liu, M. Zhang, *J. Solid State Chem.*, 2013, **203**, 60-67.

[6] F. Luan, G. Wang, Y. Ling, X. Lu, H. Wang, Y. Tong, X.-X. Liu, Y. Li, *Nanoscale*, 2013, **5**, 7984-7990.

[7] X. Mao, T.A. Hatton, G.C. Rutledge, *Curr. Org. Chem.*, 2013, **17**, 1390-1401.

[8] X. Liu, S. Shi, Q. Xiong, L. Li, Y. Zhang, H. Tang, C. Gu, X. Wang, J. Tu, *ACS Appl. Mater. Inter.*, 2013, **5**, 8790-8795.

[9] A.L.M. Reddy, S.R. Gowda, M.M. Shaijumon, P.M. Ajayan, *Adv. Mater.*, 2012, **24**, 5045-5064.

[10] G. Wang, L. Zhang, J. Zhang, *Chem. Soc. Rev.*, 2012, **41**, 797-828.

[11] Z.-S. Wu, G. Zhou, L.-C. Yin, W. Ren, F. Li, H.-M. Cheng, *Nano Energy*, 2012, **1**, 107-131.

[12] Y. Yue, P. Han, S. Dong, K. Zhang, C. Zhang, C. Shang, G. Cui, *Chin. Sci. Bull.*, 2012, **57**, 4111-4118.

[13] C. Wu, S. Deng, H. Wang, Y. Sun, J. Liu, H. Yan, *ACS Appl. Mater. Inter.*, 2014, **6**, 1106-1112.

[14] Z. Yang, F. Xu, W. Zhang, Z. Mei, B. Pei, X. Zhu, *J. Power Sources*, 2014, **246**, 24-31.

[15] M. Khairy, S. A. El-Safty, *RSC Adv.*, 2013, **3**, 23801-23809.

[16] Q. Yang, Z. Lu, X. Sun, J. Liu, *Sci. Rep.*, 2013, **3,** 3537.

[17] X. Zhang, Y. Zhao, C. Xu, *Nanoscale*, 2014, **6**, 3638-3646.

[18] X. Sun, H. Wang, Z. Lei, Z. Liu, L. Wei, *RSC Adv.*, 2014, **4**, 30233-30240.

[19] C. Wei, P.S. Lee, Z. Xu, *RSC Adv.*, 2014, **4**, 31416-31423.

[20] G. Zhu, Z. He, J. Chen, J. Zhao, X. Feng, Y. Ma, Q. Fan, L. Wang, W. Huang, *Nanoscale*, 2014, **6**, 1079-1085.

[21] L. Huang, D. Chen, Y. Ding, Z.L. Wang, Z. Zeng, M. Liu, *ACS Appl. Mater. Inter.*, 2013, **5**, 11159-11162.

[22] Q. Wang, L. Jiao, H. Du, Y. Wang, H. Yuan, *J. Power Sources*, 2014, 245, 101-106.

[23] F. Zhang, T. Zhang, X. Yang, L. Zhang, K. Leng, Y. Huang, Y. Chen, *Energy & Environ. Sci.*, 2013, **6**, 1623-1632.

[24] H. Wang, Q. Gao, L. Jiang, *Small*, 2011, **7**, 2454-2459.

[25] C. Yuan, J. Li, L. Hou, X. Zhang, L. Shen, X.W. Lou, *Adv. Funct. Mater.*, 2012, **22**, 4592-4597.

[26] G. Zhang, X.W. Lou, *Adv. Mater.*, 2013, **25**, 976-979.

[27] R. Ding, L. Qi, H. Wang, *J. Solid State Electrochem.*, 2012, **16**, 3621-3633.

[28] Z. Wang, Y. Zhang, Y. Li, H. Fu, *RSC Adv.*, 2014, **4**, 20234-20238.

[29] L. Hu, L. Wu, M. Liao, X. Hu, X. Fang, *Adv. Funct. Mater.*, 2012, **22**, 998-1004.

[30] J. Xiao, S. Yang, *RSC Adv.*, 2011, **1**, 588-595.

[31] X.Y. Liu, Y.Q. Zhang, X.H. Xia, S.J. Shi, Y. Lu, X.L. Wang, C.D. Gu, J.P. Tu, *J. Power Sources,* 2013, **239**, 157-163.

[32] L. Li, S. Peng, Y. Cheah, P. Teh, J. Wang, G. Wee, Y. Ko, C. Wong, M. Srinivasan, *Chem- Eur. J.*, 2013, **19**, 5892-5898.

[33] W. Liu, C. Lu, K. Liang, B.K. Tay, *J. Mater. Chem. A*, 2014, **2**, 5100-5107.

[34] M. Zhi, A. Manivannan, F. Meng, N. Wu, *J. Power Sources*, 2012, **208**, 345-353.

[35] C. Shang, S. Dong, S. Wang, D. Xiao, P. Han, X. Wang, L. Gu, G. Cui, *ACS Nano*, 7 2013, **7**, 5430-5436.

[36] Z. Tang, C.-h. Tang, H. Gong, *Adv. Funct. Mater.*, 2012, **22**, 1272-1278.

[37] J. Zhang, X. Wang, J. Ma, S. Liu, X. Yi, *Electrochim. Acta*, 2013, **104**, 110-116.

[38] F. Zhang, C. Yuan, J. Zhu, J. Wang, X. Zhang, X.W. Lou, *Adv. Funct. Mater.*, 2013, **23**, 3909-3915.

[39] J. Liu, J. Essner, J. Li, *Chem. Mater.*, 2010, **22**, 5022-5030.

[40] Z. Fan, J. Chen, K. Cui, F. Sun, Y. Xu, Y. Kuang, *Electrochim. Acta*, 2007, **52**, 2959-2965.

[41] A.L.M. Reddy, S. Ramaprabhu, *J. Phys. Chem. C*, 2007, **111**, 7727-7734.

[42] P.-C. Chen, G. Shen, Y. Shi, H. Chen, C. Zhou, *ACS Nano*, 2010, **4**, 4403-4411.

[43] A.L.M. Reddy, M.M. Shaijumon, S.R. Gowda, P.M. Ajayan, *Nano Lett.*, 2009, **9**, 1002-1006.

[44] K. He, Q. Wu, X. Zhang, X. Wang, *J. Electrochem. Soc.*, 2006, **153**, A1568-A1574.

[45] R.R. Salunkhe, K. Jang, S.-w. Lee, S. Yu, H. Ahn, *J. Mater. Chem.*, 2012, **22**, 21630-21635.

[46] W. Yang, Z. Gao, J. Wang, J. Ma, M. Zhang, L. Liu, *ACS Appl. Mater. Inter.*, 2013, **5**, 5443-5454.

[47] L.-H. Su, X.-G. Zhang, Y. Liu, *J. Solid State Electrochem.*, 2008, **12**, 1129-1134.

[48] H. Jiang, P.S. Lee, C. Li, *Energy & Environ. Sci.*, 2013, **6**, 41-53.

[49] M. Prabu, K. Ketpang, S. Shanmugam, *Nanoscale*, 2014, **6**, 3173-3181.

[50] R.R. Salunkhe, K. Jang, H. Yu, S. Yu, T. Ganesh, S.-H. Han, H. Ahn, *J. Alloys Compd.*, 2011, **509**, 6677-6682.

[51] R. Ding, L. Qi, M. Jia, H. Wang, *Electrochim. Acta.*, 2013, **107**, 494-502.

[52] H. Chen, J. Jiang, L. Zhang, T. Qi, D. Xia, H. Wan, *J. Power Sources*, 2014, **248**, 28-36.

[53] H.-W. Wang, Z.-A. Hu, Y.-Q. Chang, Y.-L. Chen, H.-Y. Wu, Z.-Y. Zhang, Y.-Y. Yang, *J. Mater. Chem.*, 2011, **21**, 10504-10511.

[54] H. Wang, X. Wang, *ACS Appl. Mater. Inter.*, 2013, **5**, 6255-6260.

[55] W. Zhou, D. Kong, X. Jia, C. Ding, C. Cheng, G. Wen, *J. Mater. Chem. A* 2014, **2**, 6310–6315

[56] X. Wang, X. Han, M. Lim, N. Singh, C. L. Gan, M. Jan, *J. Phys. Chem. C* 2012, **116**, 12448-12454..

[57] Z. Li, Z. Xu, H. Wang, J. Ding, B. Zahiri, C. M. B. Holt, X. Tan, D. Mitlin, *Energy & Environ. Sci.*, 2014, **7**, 1708-1718

Figures and Captions:

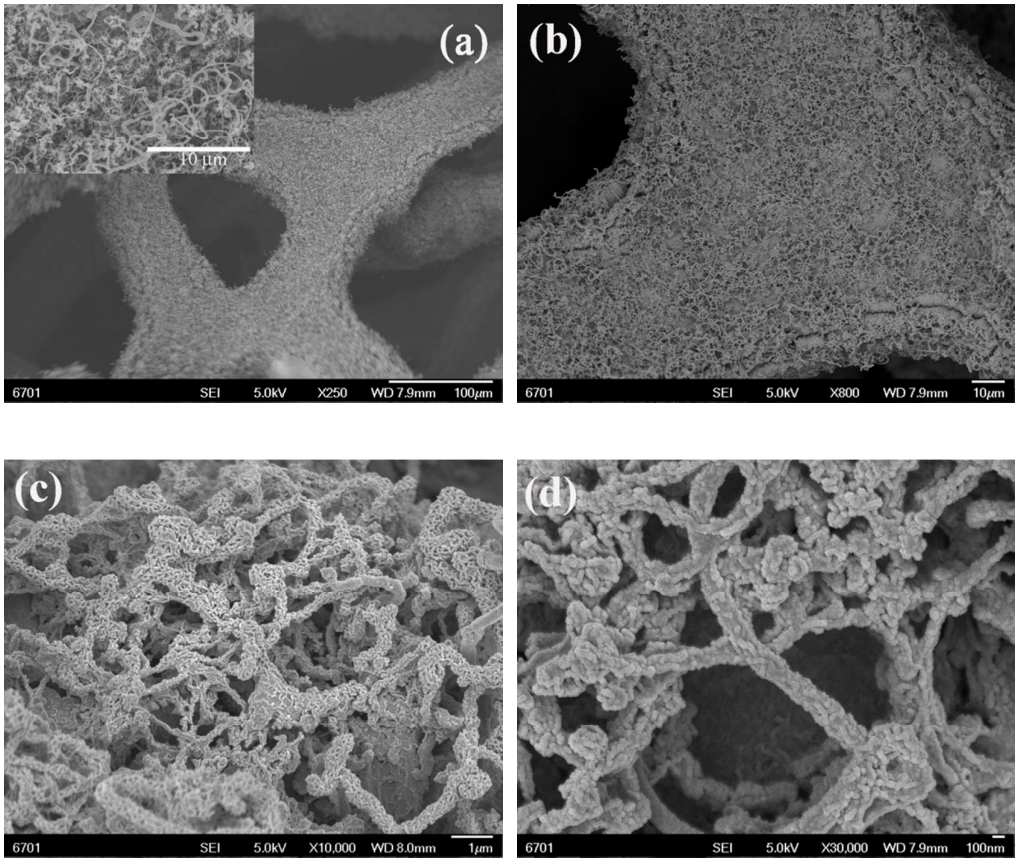

Figure 1 (a) FESEM image of hairy-like CNTs grown on NF. (b-d) FESEM images of as-prepared 3D $NiCo_2O_4$/CNT core-shell network structure with different magnifications.

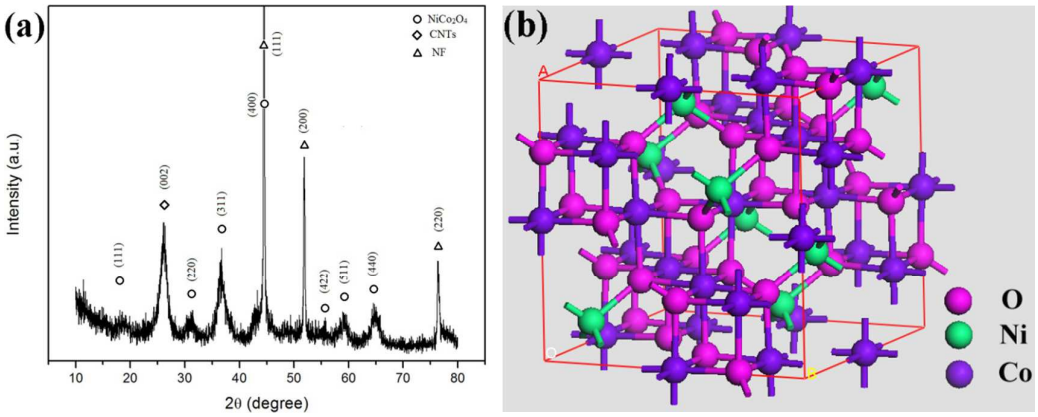

Figure 2 XRD pattern (a) and crystal structure (b) of $NiCo_2O_4$ on CNT/NF substrate.

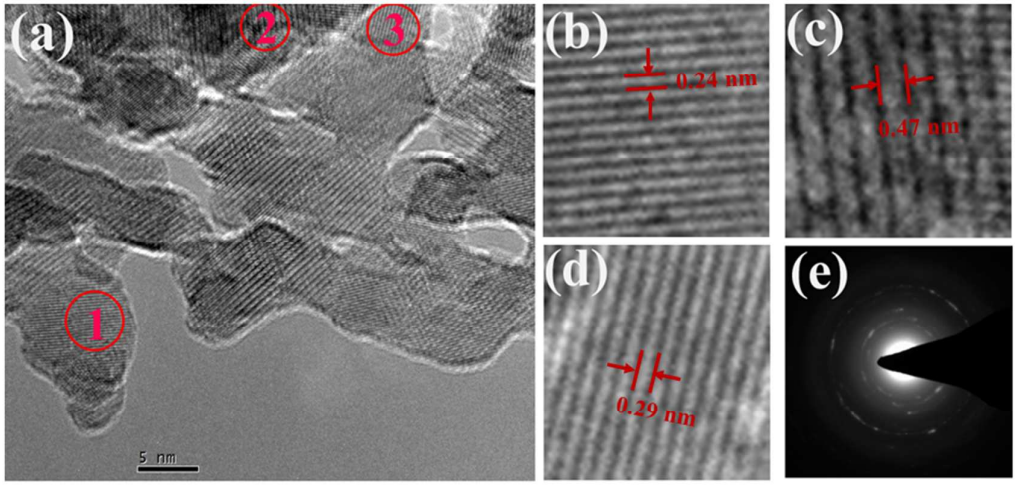

Figure 3 (a-d) HRTEM images and (e) SAED of $NiCo_2O_4$ nanoparticles on CNT/NF substrate. Images of (b-d) are the enlargement of regions 1, 2 and 3 in panel a, respectively.

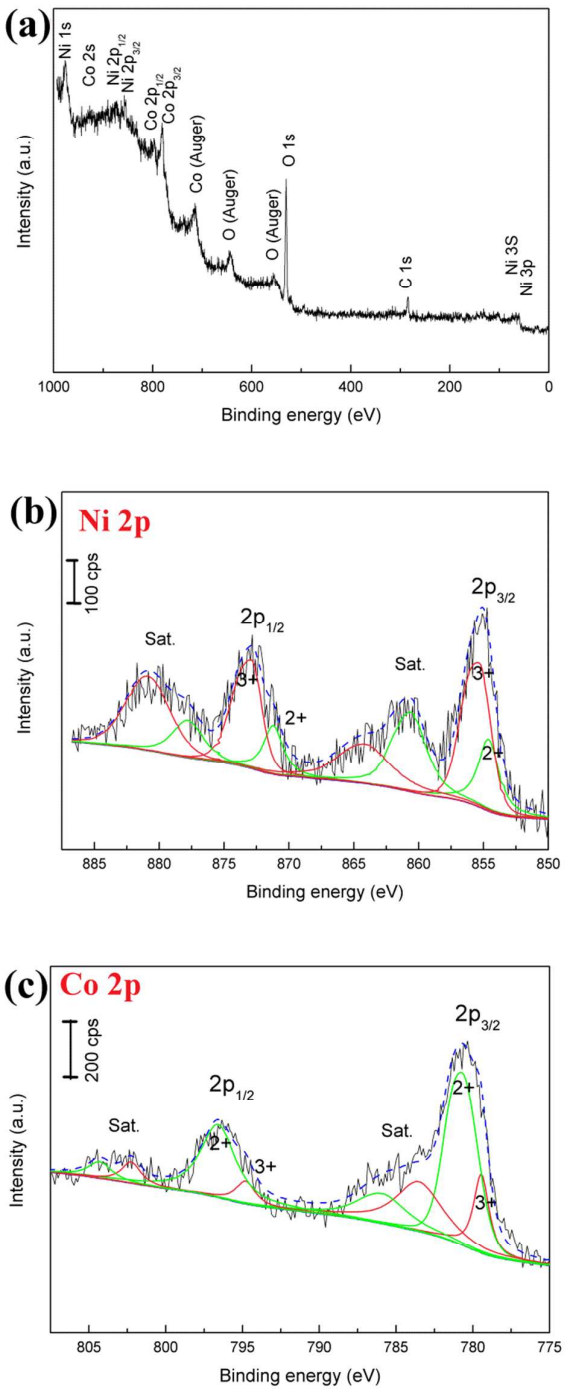

Figure 4 XPS spectra of $NiCo_2O_4$: (a) survey scan, (b) Ni 2p and (c) Co 2p core levels.

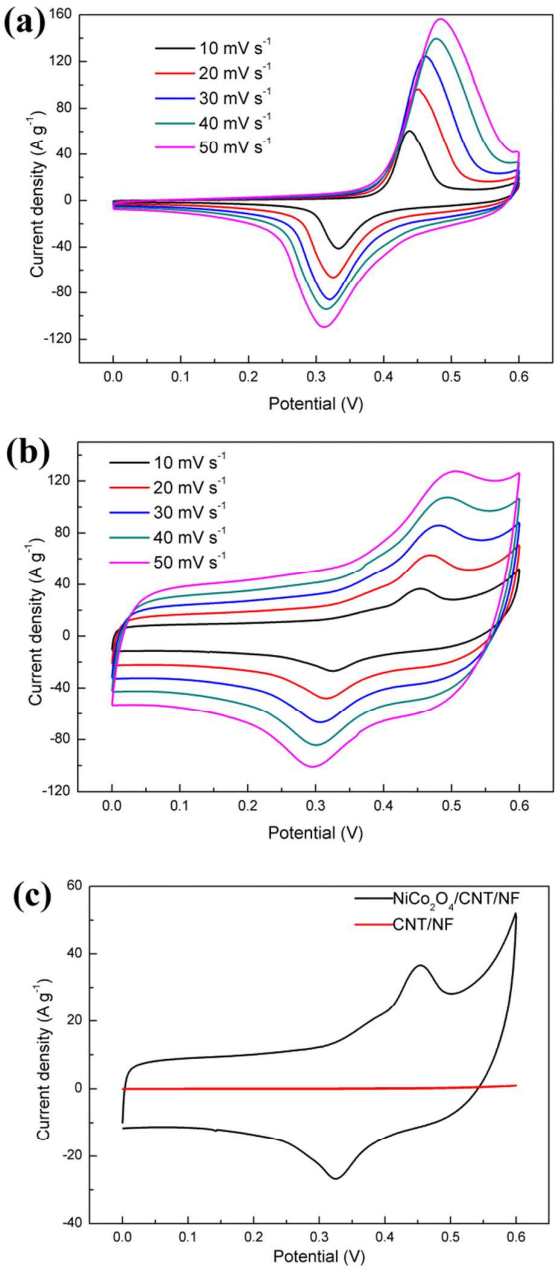

Figure 5 CV curves of (a) $NiCo_2O_4$/NF electrode and (b) $NiCo_2O_4$/CNT/NF electrode at sweep rates ranging from 10-50 mV s^{-1}. (c) comparison of CV curves of $NiCo_2O_4$/CNT/NF electrode and CNT/NF substrate at sweep rate of 10 mV s^{-1}.

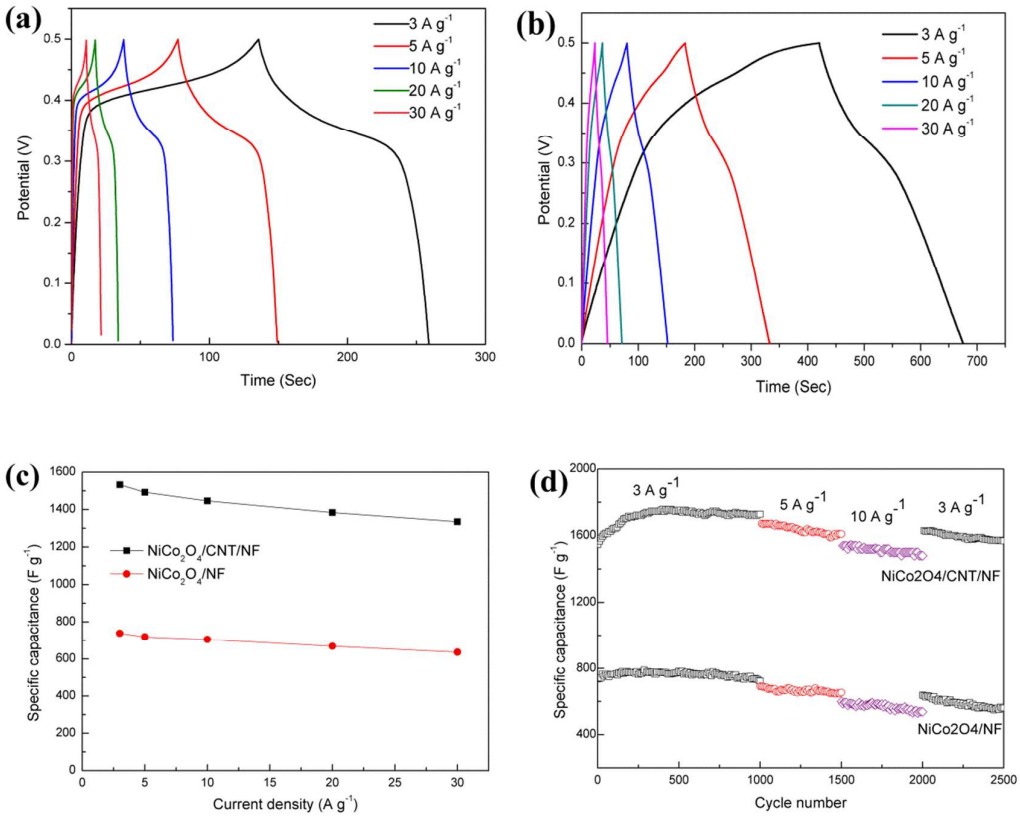

Figure 6 CDC curves of (a) $NiCo_2O_4$/NF electrode and (b) $NiCo_2O_4$/CNT/NF electrode at various current densities. (c) comparison of the capacitance of two electrodes at various current densities. (d) Cycling stability of the $NiCo_2O_4$/CNT/NF electrode at various current densities in 1 M KOH solution.

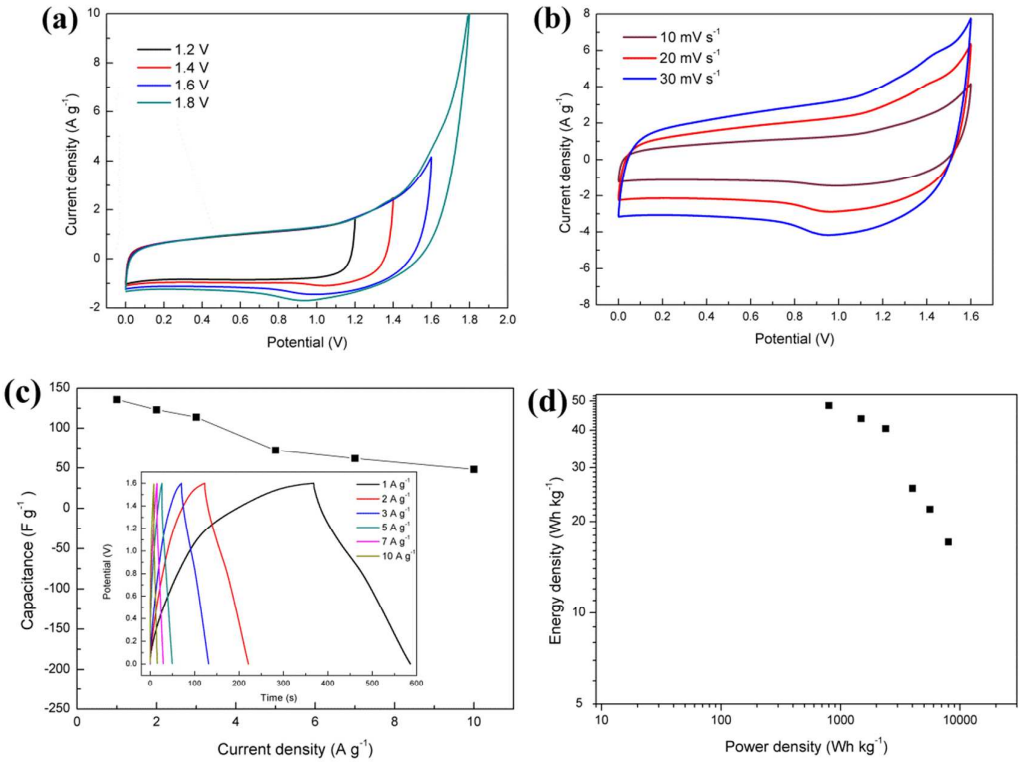

Figure 7 Electrochemical evaluation of the asymmetric supercapacitor device: (a) CV curves at various potential windows with a scan rate of 10 mV s^{-1}. (b) CV curves at various scam rates. (c) Capacitance of at different current densities (Inset image is corresponding CDC curves). (d) Ragone plot related to energy density and power density.

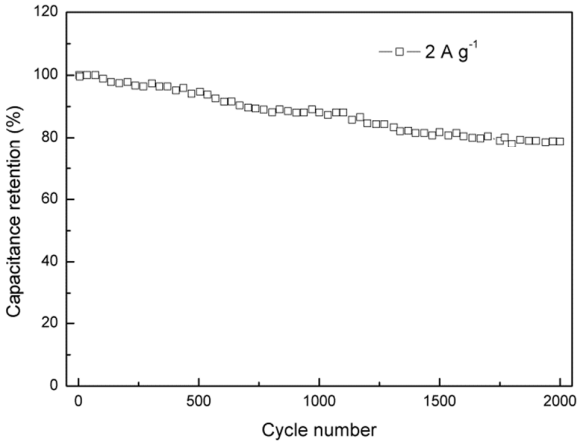

Figure 8 Cycling stability of the asymmetric device measured at a current density of 2 A g^{-1}.